CrossMark
click for updates

Bimodal NdNiAl and NdFeB hybrid catalytic and magnetic nanoparticles laminated on Fe foam: catalytic conversion of CO + 3H$_2$ to CH$_4$†

Sang Hoon Kim,*[a] Joonphil Choi,[b] Jaecheol Yun[a] and Eun-wook Jeong[a]

For the production of CH$_4$ from CO hydrogenation, a hybrid foam with high catalytic activity and strong magnetic bonding ability was fabricated by electrospraying and co-sintering Nd-doped NiAl catalytic nanoparticles and NdFeB magnetic nanoparticles over a Fe foam. When the NdNiAl nanoparticles were uniformly distributed over a NdFeB nanoparticles support, they exhibited exceedingly high catalytic activity, selective conversion and stable adhesion. In particular, bimodal NdNiAl–NdFeB hybrid nanoparticles (with a ratio of 85.0 to 15.0 wt%) immobilized on Fe foam exhibited a high CO to CH$_4$ conversion rate, with a TOF value of 1.1 s^{-1} and a CH$_4$ selectivity value of 77.1% at a specific temperature of 260.0 °C. This improved catalytic behavior was attributed to the enhanced uniform dispersion of NdNiAl nanoparticles over a NdFeB nanoparticles support. At the same time, the NdFeB nanoparticles had high hydrogen absorptivity, which helped adjacent NdNiAl nanoparticles activated with CO to be hydrogenated and produce CH$_4$.

1. Introduction

The exploitation of shale gas has ignited a great demand for the research and development of technologies to convert natural gas into transportable and more valuable chemicals and fuels.[1–3] The mixture of CO and H$_2$ is a rich component of shale gas, and converting the two natural gases into CH$_4$ (CO + 3H$_2$ → CH$_4$ + H$_2$O, $\Delta H_{298}^0 = -206$ kJ mol^{-1}) is useful for the current exploitation practices with regard to the effectiveness and efficiency of fuel productivity.[4] Commercial scale production of CH$_4$ is carried out using an adiabatic multi-tubular reactor packed with an excess amount of catalyst at an inlet feed temperature of 300–350 °C.[4] However, owing to the excessive exothermic nature of the reaction, the reaction temperature is known to increase to 800 °C at a certain section of the reactor bed, and this hot zone gradually moves toward the downstream section during operation.[5] Moreover, the product mixture inside the reactor contains a significant amount of steam which accelerates the thermal deactivation (oxide and/or carbide) of the catalyst. Therefore, for practical application of a catalyst, its durability under such high-severity conditions (high temperature with steam) is as important as the initial activity.

There has been a great deal of research and advances in general knowledge about stable catalyst materials including bimetallic PtNi, AuPt, hybrid Pt/ZnAl$_2$O$_4$, Au/Ni, Pd/TiO$_2$, Pd/CeO$_2$ and intermetallic Pt$_3$Cu compounds.[6–11] However, the use of noble or rare earth metals leads to the problem of high cost. Moreover, an intermediate supporter is needed to tightly consolidate the stable catalyst on the template.[8,9] In this respect, the activation of cheap catalytic nanostructures in the support of facilitating magnetic nanostructures provides an attractive and effective route. Among conventional catalyst materials, nickel aluminide (NiAl) is used in a variety of catalytic applications and is known to operate well beyond the catalytic temperature of pure Ni or Al.[12–14] In addition, NiAl is susceptible to chemical modification using specific dopants, and significantly improves magnetic and mechanical strength, corrosion and oxidation resistance, and thermal behavior of products.[15–19] Compared to other noble or rare earth metals, Nd is an effective dopant from the aspect of its high catalysis and strong magnetism; although Pt, Ti, Ir, and Ru are commonly used as catalytic dopants in the synthesis of the NiAl RANEY® catalyst.[20–26] Meanwhile, magnetic NdFeB also has several superior properties that have mainly been exploited in electrochemical or magnetic devices.[23,27] This is primarily due to its excellent saturation magnetization and coercivity values.[23,27] In particular, NdFeB nanostructures can form a facilitating support that allows the catalytic nanostructures to gain the advantage of uniform distribution; as a result becoming more catalytically active than single mode catalytic nanostructures. NdFeB nanostructures also show high affinity toward hydrogen; thus, the hydrogen penetrates the interstitial sites of the NdFeB lattice,

[a]*Powder Technology Department, Korea Institute of Materials Science, Changwon 51508, Republic of Korea. E-mail: sanghooni79@kims.re.kr; Tel: +82 010 9111 6620*

[b]*Department of Mining and Materials Engineering, McGill University, 3610 University Street, Montreal, QC, H3A 0C5, Canada*

† Electronic supplementary information (ESI) available. See DOI: 10.1039/c7ra00940b

and the Nd hydride develops a Nd-rich phase during the hydrogenation.[27,28] Thus, the magnetic nanostructures are very suitable as an assisting catalyst for the hydrogenation of CO to CH₄, when being interacted together with the described catalytic nanostructures, which have high reactivity with CO.

The performance of catalytic nanostructures is mainly dependent on the degree of exposure of active sites.[29,30] Thus, many different techniques have been designed to obtain uniform distribution of the nanostructures on a template initially, and to avoid their agglomeration during catalytic activity.[29,30] A number of porous templates such as zeolites, metal oxides, polymers, carbon nanotubes, and graphene arrays have been designed to restrain the aggregation of nanostructures.[31–34] Metal foam has been emerging as a class of promising and multi-functional framework templates owing to their high porosity, large surface area, chemical tenability, and thermal stability.[12,35,36] Given their similarity to zeolites, metal foam made by loading nanostructures into the pores of the template is expected to allow the control of limited nanostructure growth in confined cavities and produce evenly distributed structures, which should improve catalytic activity.[12,35,36] In addition to its three-dimensional pore structures, the presence of the strong metallic links and great mechanical strength can also cause the metal foam to possess unique advantages over other template materials.[12,35,36]

Herein, we report for the first time the preparation of Nd-doped NiAl catalytic nanoparticles supported by NdFeB magnetic nanoparticles and the application of these bimodal nanoparticles over a Fe foam for hydrogenation of CO to CH₄. First, Nd is used as a dopant to NiAl RANEY® nanoparticles. Then, the role of the NdFeB nanoparticles as an intermediate supporter and assisting catalyst is also investigated in terms of their distribution morphology and hydrogenation performance. Consequently, our study finds that NdNiAl nanoparticles supported with NdFeB nanoparticles synergistically improve catalytic activity compared to either single mode NdNiAl nanoparticles or conventional NiAl nanoparticles. The uniform distribution of NdNiAl nanoparticles supported by NdFeB nanoparticles over a Fe foam plays a critical role in maximizing the activity of the catalyst sites. Morphologic evolution is also observed after sintering both NdNiAl and NdFeB nanoparticles over the Fe foam; the morphology varies with the intrinsic magnetic strength of each hybrid foam constituent, in particular depending on the concentration ratio between catalytic and magnetic nanoparticles. Having these NdNiAl–NdFeB hybrid nanoparticles (ratio of 85.0 to 15.0 wt%) on the Fe foam, leads to a highly invariable curvature, a very stable structure, and the large surface area necessary for high catalytic activity.

2. Experimental section

2.1. Syntheses of NdNiAl and NiAl nanoparticles

Nickel chloride (NiCl₂, ≥99.99%, Sigma Aldrich, USA), neodymium chloride (NdCl₃, ≥99.99%, Sigma Aldrich, USA), 1,3,5-trimethylbenzene (C₆H₃(CH₃)₃, ≥98%, Sigma Aldrich, USA), lithium aluminum hydride (LiAlH₄, ≥97.0%, Sigma Aldrich, USA), and pyridine (C₅H₅N, ≥99.9%, Sigma Aldrich,

USA) were used as-received. All nanoparticles were prepared by dissolving each element at the intended ratio, in the presence of 1,3,5-trimethylbenzene, by adding LiAlH₄. In a typical experiment, NiCl₂ (15.55 g, 0.12 mol) in the presence and absence of NdCl₃ (0.28 g, 0.0011 mol) were placed in a round three-neck flask containing 120 mL of 1,3,5-trimethylbenzene. This was followed by addition of LiAlH₄ (3.44 g, 0.091 mol) under continuous stirring and argon gas, and continuation of the reaction for 16 h at 164 °C. The as-synthesized nanoparticles in pyridine were centrifuged at 4000 rpm for 15 min. Then, they were washed three times with pyridine and heat-treated in an H₂ atmosphere for 12 h at 700 °C to remove any possible residual organic or halide impurities, particularly minimizing the amount of chloride. Before being exposed to air, the nanoparticles were further annealed under a stream of H₂ at 250 °C for 1 h. After the reduction, the nanoparticles were stored in a nitrogen box.

2.2. Fabrication of NdFeB nanoparticles

Strip-cast Nd₂Fe₁₄B ribbons (Santoku Corporation, Japan) were hydrogenated and then jet-milled (Toner Fluidized Bed Opposed Jet Mill, HOSOKAWA ALPINE Aktiengesellschaft, Japan) in a stainless steel container using liquid nitrogen. The jet-milled Nd₂Fe₁₄B powders, with a size range of 4.2–8.7 μm, were fabricated using a plasma treatment method (Tekna-80, Tekna Plasma Systems Inc., Canada). The obtained NdFeB nanoparticles (9.2–187.4 nm) had a mostly amorphous structure. All experiments were conducted in a glove box in an inert atmosphere; the reason that the NdFeB nanoparticles were fabricated by the physical method of plasma treatment instead of a chemical method using a reducing agent, was that this physical method involved less surface oxidation and more phase separation.

2.3. Fabrication of Fe foam

Fe foam was prepared by a slurry coating process. After Fe powders (Fe, ≥99.9%, <10 μm, Sigma Aldrich, USA) were blended with polyvinyl alcohol (PVA 1500, Junsei, Japan) to fabricate an Fe slurry, the Fe slurry was coated on polyurethane foam. The coated foam was sintered at 1250 °C under a flow of H₂ gas to remove the polyurethane and to reduce any oxidized Fe powders. The Fe foam had the proportions 1.8 × 1.8 × 0.3 cm³ and porosity of 91.2%.

2.4. Consolidation of NdNiAl–NdFeB hybrid nanoparticles with Fe foam

The NdNiAl–NdFeB hybrid nanoparticles with the intended composition, as shown in Table 1, were sprayed onto the Fe foam using an electrostatic spray system with a high precision multichannel dispenser (ISM936D, ISMATEC, Germany). About 0.10 g of hybrid nanoparticles was sprayed onto the Fe foam and then consolidated at 700 °C for 12 h. Before being exposed to air, the foam was annealed under H₂ at 250 °C for 1 h, and then oriental magnetization of the NdNiAl and NdFeB nanoparticles was conducted to induce maximum magnetic strength.

Table 1 Chemical composition and oxygen affinity of hybrid foam constituents

	Fe foam (wt%)	NiAl NPs (wt%)	NdNiAl NPs (wt%)	NdFeB NPs (wt%)	O amount (wt%)
A	100.0	0.0	0.0	0.0	0.184
B	0.0	100.0	0.0	0.0	2.410
C	0.0	0.0	100.0	0.0	2.852
D	0.0	0.0	0.0	100.0	0.687
E	0.0	0.0	85.0	15.0	2.502
F	0.0	0.0	50.0	50.0	1.768
G	0.0	0.0	15.0	85.0	1.010

2.5. Catalytic activity and magnetic strength measurements of NdNiAl and NiAl nanoparticles

The catalytic activity of the hybrid foam was determined using a catalyst analyzer (BELCAT-B, MicrotracBEL Corp., Japan). The magnetic strength of the nanoparticles was measured using a vibrating sample magnetometer (VSM, 7400 Series VSM, Lake Shore Cryotronics, Inc., USA). Before the catalytic reaction, the hybrid foam was reduced at 250 °C under a flow of H_2 (0.1 L min^{-1}) for 1 h and then cooled to room temperature. Then, reactant gas of the composition 1CO to $3H_2$ was admitted in a flow reactor loaded with the experimental catalyst. The reactant gas composition was 20% CO, 60% H_2, and 20% He (carrier gas). The deactivated hybrid NdNiAl–NdFeB nanoparticles over Fe foam were reactivated using the reducing gas composition of 80% H_2 and 20% He at a temperature of 700 °C for 12 h. The total gas flow rate was 20 mL min^{-1} regulated by mass flow controllers (BROOKS instrument).[4,37] The gas released during the catalytic reaction was directed into a gas chromatograph (GC, iGC7200, DS Science, Korea) with a thermal conductivity detector (TCD) to quantitatively measure the extent of its hydrogenation. CO hydrogenation was carried out until 100% conversion: the operating temperature was varied from 100 to 500 °C to obtain the optimum activation energy, which also informed the optimum catalytic temperature. The space velocity of the reaction was 10 000 h^{-1}. Different sets of experiments were performed for comparison. The turnover frequency rate of the six samples with different loading and concentration ratios was calculated, based on the chemisorption and CO conversion data obtained by the hydrogenation via the flow reactor. The turnover rate of CO hydrogenation is given by:

$$\text{TOF} = [\text{no. of hydrogenated CO atoms}] / [\text{no. of active catalyst atoms}] \quad (1)$$

where [no. of active catalyst atoms] = [metal surface area (m^2 g^{-1})] × [sample weight (g)] × [atomic density of catalyst surface], and [no. of hydrogenated CO atoms] is calculated using the ideal gas equation ($PV = nRT$, P = gas pressure (2.0 atm), V = flow rate (2.0 mL min^{-1}), and R = gas constant (0.082 L atm mol^{-1} K^{-1})).[38–40]

2.6. Characterizations

Total concentrations of carbon and oxygen were determined using a C/S analyzer (CS-800, ELTRA GmbH, Germany) and an N/O analyzer (NO-900, ELTRA GmbH, Germany) to determine the carbon and oxygen content of the NdNiAl nanoparticles, NiAl nanoparticles, NdFeB nanoparticles, and Fe foam.[41–43] Scanning electron microscopy (SEM) with energy dispersive X-ray spectroscopy (EDS) was conducted to obtain surface images of the foam using a scanning electron microscope (SEM, JSM-6610/LV, JEOL, Japan). The size of the nanoparticles was analyzed using a particle-size analyzer (LA-960 Laser Particle Size Analyzer, Horiba Scientific, Japan) that included a laser-induced scattering measurement detector. Morphology and size of the nanoparticles were observed using a transmission electron microscope (TEM, JEM-ARM200F, JEOL, Japan) equipped with EDS at an acceleration voltage of 200 kV. The nanoparticles were collected on holey carbon-coated copper TEM grids, and were imaged without further preparation. X-ray diffraction patterns were recorded on a diffractometer (XRD, D/ Max-2500VL/PC, Rigaku International Corporation, Japan) equipped with a Cu K$_\alpha$ radiation source (λ = 0.154 nm) operating at 250 kV and 40 mA. X-ray photoelectron spectroscopy measurements were performed with a spectrophotometer (XPS, Quantera SXM, ULVAC-PHI, Japan) and XPSPEAK 4.1 software. Thermo-gravitational and differential scanning calorimetric measurements were obtained in argon at a temperature rising in increments of 5 °C min^{-1}, using a calorimeter (TGA-DSC, Q100, TA Instrument, USA). The specific surface area and pore size distribution were determined by N_2 adsorption/desorption isotherms based on the Brunauer–Emmett–Teller (BET) method using the analysis port of a Physisorption and Chemisorption Analyzer (Autosorb-iQ, Quantachrome Instrument, USA).

3. Results and discussion

3.1. Comparison of electron microscopy images of as-synthesized NdNiAl nanoparticles and as-fabricated NdFeB nanoparticles

Nd-Doped NiAl catalytic nanoparticles, NiAl RANEY® nanoparticles and NdFeB magnetic nanoparticles were characterized by TEM to identify the morphology and phase of the catalytic and magnetic nanoparticles responsible for the catalytic activity and magnetic strength. Fig. 1 provides TEM and HRTEM images of the NdNiAl nanoparticles that were synthesized. The synthesized NdNiAl nanoparticles (Fig. 1a) were mostly spherical, with an average size of 21.8 nm. HRTEM images, shown in Fig. 1b and c, revealed the morphology and crystallinity of the NdNiAl nanoparticles. From the HRTEM image (Fig. 1b), it was determined that the lattice fringe measurements of the primary
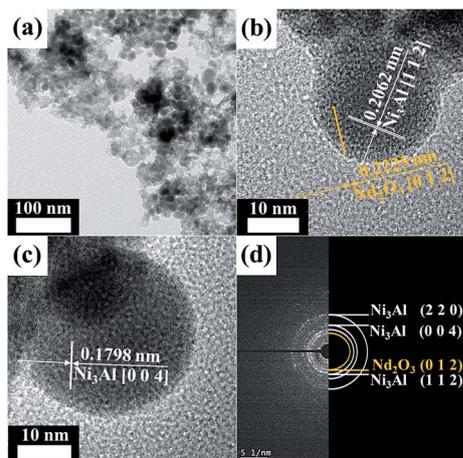
Fig. 1 TEM images and SAED pattern of NdNiAl nanoparticles: the NdNiAl nanoparticles were mostly present in intermetallic compounds.

nanoparticles were 0.2062 and 0.2225 nm, which is close to the [1 1 2] and [0 1 2] lattice planes of Ni_3Al and Nd_2O_3 with tetragonal and hexagonal structures, respectively.[44,45] The HRTEM image in Fig. 1c revealed a lattice fringe measurement of 0.1798 nm between the two white highlighted lines, which corresponded to the inter-planar distance [0 0 4] of Ni_3Al in a tetragonal structure (JCPDS #501265), with a measurement error of <1.0%. Fig. 1d exhibits the selected area electron diffraction (SAED) pattern obtained from a random assembly of as-synthesized NdNiAl nanoparticles; thus, the main ($h\ k\ l$) planes of Ni_3Al in the tetragonal structure were also found in the diffraction ring pattern whose nanoparticles had a polycrystalline structure.

Fig. 2 is a TEM image of the NdFeB nanoparticles prepared by plasma treatment using an evaporation–condensation method. It was found that the resultant NdFeB nanoparticles (Fig. 2a) had an average diameter of 93.1 nm. The nanoparticles were also aggregated to a certain extent. Fig. 2b provides an
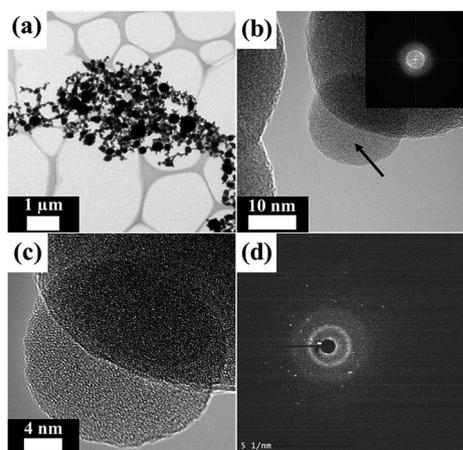

Fig. 2 TEM images and SAED pattern of NdFeB nanoparticles: the NdFeB nanoparticles were mostly present in an amorphous structure.

HRTEM image of the NdFeB nanoparticles; the inset provides a corresponding FFT image. The diffraction pattern indicated by the arrow in the FFT image determined that the nanoparticles were mostly present in an amorphous structure. The HRTEM image (Fig. 2c) also shows that the resultant amorphous NdFeB nanoparticles have a superimposed periodic structure. Fig. 2d exhibits a corresponding SAED pattern obtained by directing the incident electron beam at the nanoparticles having an amorphous structure. After all, these results indicate that a high-density, internal, amorphous structure occurred when plasma treatment was applied for nanofabrication.

The EDS mapping analysis (ESI Fig. 2†) provided relatively good confirmation of the coexistence of all elements in the as-synthesized NdNiAl nanoparticles. Comparatively, the EDS mapping results for the as-fabricated NdFeB nanoparticles with different elemental compositions are shown in ESI Fig. 3†. In particular, a combined mapping analysis image of NdFeB nanoparticles revealed that they exhibited phase separation even though the plasma treatment method was effective at imparting an amorphous structure to the nanoparticles.

3.2. Spectroscopic characterization of NdNiAl, NiAl, and NdFeB nanoparticles, and Fe foam

The XRD patterns of the Nd-doped NiAl catalytic nanoparticles and the NiAl RANEY® nanoparticles are shown in Fig. 3a. The XRD diffraction peaks appearing at $2\theta = 24.60$, 35.60, 43.92, and 50.76° were indexed as the (0 0 2), (1 1 0), (1 1 2), and (0 0 4) planes, respectively, in the intermetallic Ni_3Al compound, having a body-centered tetragonal structure (JCPDS #501265). It was clear that when Nd was added to the NiAl nanoparticles, the peak intensities of (2 2 0), (3 1 1), and (4 2 2), at 31.61, 37.25, and 56.29°, appeared due to the presence of $NdAl_2$. Other peaks were also present, indicating that Nd_2O_3 had formed. Subsequently, the XRD patterns showed that the intermetallic Ni_3Al and $NdAl_2$ compounds of the NdNiAl nanoparticles turned into more stable phases after heat treatment at 700 °C. However, no diffraction peaks of nickel oxides or nickel hydroxides were detected, indicating that the purer phase of Ni_3Al was prepared under the present conditions. As can be seen in Fig. 3b, the XRD patterns of the NdFeB magnetic nanoparticles show a significant decrease in the intensity of the diffraction peak at 26.2°, indicating that the crystallinity of the NdFeB nanoparticles was almost completely changed to a more amorphous structure. More specifically, although the magnetic nanoparticles were not completely decomposed during the thermal hydrogenation, the simultaneous appearance of peaks for NdH_{2+x}, α-Fe, and FeB_2 denoted the partial hydrogenation of NdFeB nanoparticles.[27,28] That is, the NdFeB nanoparticles exhibited phase separation into elemental Nd and Fe, according to the analysis of the peak intensity and position. These were better suited for a role as an assisting catalyst, but worse in a role as a dispersion agent, based on the strength of their magnetic force. ESI Fig. 4† shows the XRD patterns of the hybrid NdNiAl–NdFeB nanoparticles (a ratio of 85.0 to 15.0 wt%) before and after the long time period catalytic reaction of 100 h at 260.0 °C with product gases (CH_4 +

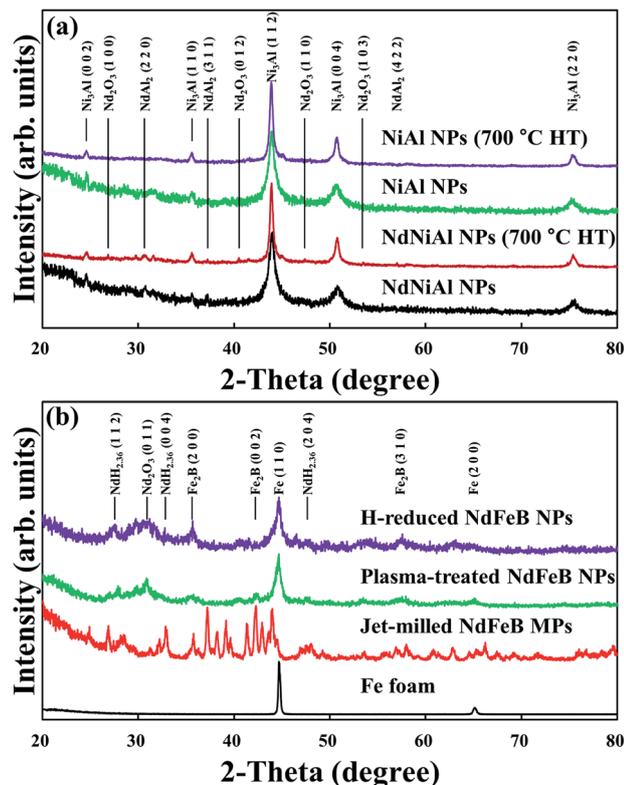**Fig. 3** XRD analysis results of (a) NdNiAl and NiAl nanoparticles prior to and after 700 °C heat treatment in flowing H_2 gas and (b) Fe foam and NdFeB micropowders and nanoparticles after being jet-milled, plasma-treated, and heat-treated in flowing H_2 gas.

H_2O). Comparatively, the crystalline structure of the catalyst was not much changed probably due to either the slow degradation of the catalyst with its unexpectedly high resistance to the carbon deposition and oxide formation or the low sensitivity of the XRD analysis to detect a small amount of deactivated (carbide or oxide form) catalyst. However, the retained carbon and oxygen amounts increased from 0.782% and 2.502% to 2.056% and 3.177%, respectively, due to the reaction (deactivation) of the catalyst with the by-products of CH_4 and H_2O. According to the research of Song and coworkers, this much degradation was inevitable under CO hydrogenation.[4]

As shown in Fig. 4, the XPS survey spectrum for the NdNiAl nanoparticles shows characteristic signals for Nd, Ni, and Al, indicating the coexistence of all the catalyst elements. The peak of $NdAl_2$ in the NdNiAl nanoparticles shifted to 977.6 eV, a lower binding energy than that of metallic Nd^0 at 980.9 eV.[46] This indicated that Nd underwent electron interaction with Al. It was inferred that the electron structure of the catalyst surface was changed due to the employment of Nd with NiAl nanoparticles. The change might affect the form of bond between the catalyst surface and CO + $3H_2$, or other reaction intermediates. In any case, the catalytic activity and selectivity of NdNiAl were improved. The peak intensity of Ni_3Al (at 852.7 eV) was higher than that of metallic Ni^0 at 858.3 eV, indicating that there was more intermetallic Ni_3Al compound than there was metallic Ni^0.[47] Each peak of Al 2p was most likely to be either an

oxidation peak, or a peak indicating formation of the intermetallic Ni_3Al compound due to exposure to air during sample preparation for the XPS experiment, and for the chemical and thermal reactions.[48] The effect of Al on Nd was significant, as can be seen in the peak of Nd. This was due to the presence of Nd, or more specifically, due to the presence of the intermetallic $NdAl_2$ compound. In addition, ESI Fig. 5† provides XPS analysis results of the as-fabricated NdFeB nanoparticles.

To confirm the necking among two different nanoparticles and their consolidation on the surface of the Fe foam during the heat treatment, DSC and TGA analysis was conducted. The DSC and TGA results, as shown in Fig. 5, indicate that the thermal behaviors of the NdNiAl nanoparticles, NiAl nanoparticles, and NdFeB nanoparticles can be compared to the thermal behavior of the standard Fe foam. In particular, the results of the NdNiAl nanoparticles show that there was necking and consolidation, at least until 344.6 °C. This might correspond to the endothermic peak of the NdNiAl nanoparticles. Obviously, the melting point of the NdNiAl nanoparticles was affected by their small size. Although the main phase of NdNiAl was Ni_3Al, the residual phases of the NdNiAl nanoparticles were completely transformed into intermetallic Ni_3Al compound by heat treatment at high temperature. This is shown by the exothermic peak at 684.0 °C.[44,49] Meanwhile, due to the amorphous structure of the NdFeB nanoparticles, the magnetic nanoparticles had a significantly broader melting point than those of the bulk materials. Furthermore, the magnetic nanoparticles, being considerably bigger (93.1 nm) than the NiAl (21.1 nm) or NdNiAl nanoparticles (21.8 nm), presented the melting range at much higher temperature, close to 740 °C. Thus, there might be sintering and necking between the NdFeB nanoparticles at the stabilization (lower) temperature of 700 °C. Because Fe foam existed in a bulk state, no significant transformation of the inert structure was noticed; thus, the TGA of the Fe foam indicated slight oxidation until at least 1000 °C. As a result, both the catalytic and magnetic nanoparticles were likely to be completely consolidated with the Fe foam through heat treatment at 700 °C, although increasing the temperature might improve this consolidation to some extent.

3.3. Microscopic characterization of NdNiAl–NdFeB hybrid nanoparticles on Fe foam

The adhesion stability of the nanoparticles on the template foam was evaluated using microscopic images (regarding surface morphology analysis, constituent concentration ratio, thermal conductivity difference, and so on).[12,35,36] It was determined that the surface microstructures were dependent on the intrinsic properties of each foam constituent with different chemical compositions. The porosity test proved that the permeability of the foam was related to its morphology, such as the number of pores per unit length, the cell shape, and the void fraction. For example, the Fe foam fabricated by the slurry coating process had 91.2% porosity, thus providing information about the morphological state of the foam, in relation to the microporous structure. The microscopic images also show the consolidated shape of the catalytic nanoparticles and/or the
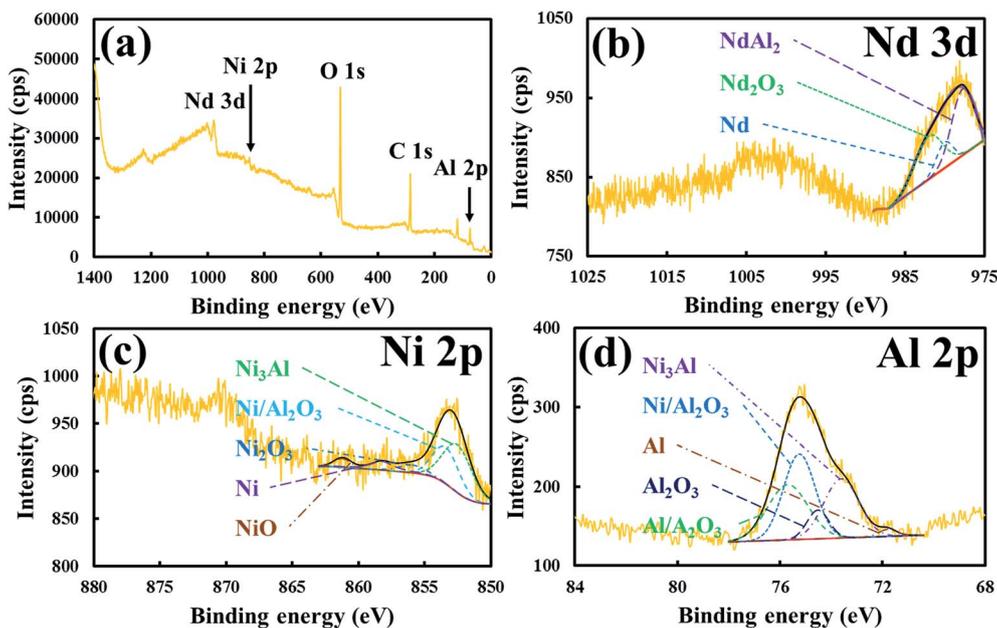
Fig. 4 XPS results for (a) survey scan, (b) Nd scan, (c) Ni scan, and (d) Al scan of NdNiAl nanoparticles.

magnetic nanoparticles on the surface of the template foam. In the porous structure of the Fe foam, there were likely to be similar, repeated cell units. It resembled a sponge, the pores were closely connected, and the struts were composed of dense dendrites. When the Nd-doped NiAl catalytic nanoparticles were uniformly distributed over the Fe foam, the catalytic foam had a peeled-off morphology, which might cause mechanical faults. The NdFeB magnetic nanoparticles consolidated over the Fe foam were found to be different in size and shape, to some extent. They exhibited clumped distribution and partial adherence due to the agglomeration induced by the strong magnetic force. However, the degree of dispersion and state of adhesion of the NdNiAl nanoparticles supported by the NdFeB nanoparticles, on top of the Fe foam, were uniform and stable, respectively.

SEM images of the as-fabricated Fe foam are provided in Fig. 6a. The structure was seen to consist of a network structure of struts in the metallic material. In particular, these struts were connected vertically and horizontally at vertices and therefore surrounded the cells. The struts typically exhibited a triangular cross section and were located between the cells. The cells had irregular, polyhedral structures. The voids inside were accessible through windows in the faces, which are also denoted as pores. In the real foam, the shape of the pores was nearly elliptical because of the accumulation of powder materials at the vertices. Furthermore, it should be remarked that many pits were distributed randomly, and no cells of the foam structure were blocked. At a higher magnification, the surface exhibited a significant number of micro-cracks, due to thermal evaporation of the polyurethane foam and necking formation between Fe powders, to which the system was inclined at high temperature. As a result, the slurry-coating method fabricated defective foam, a condition that was effective for nanoparticle dispersion.

As shown in Fig. 6b, most of the NdNiAl layers over the Fe foam peeled off due to thermal cracking, and there was a blazing effect after heat treatment at a high temperature. The shell peeling of the NdNiAl nanoparticles from the Fe foam might be due to the difference in thermal conductivity between
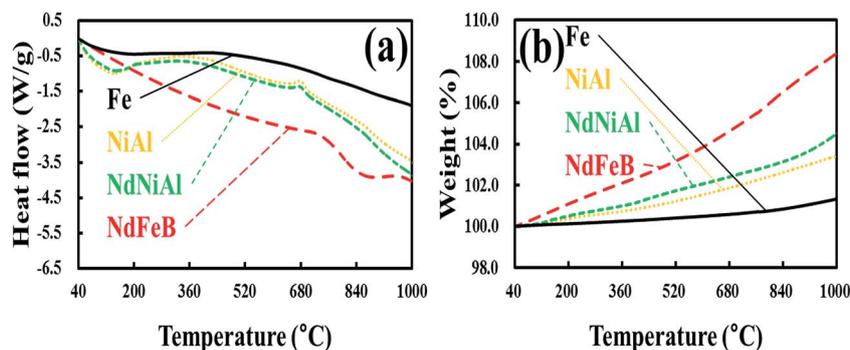

Fig. 5 DSC (a) and TGA (b) of NiAl nanoparticles, NdNiAl nanoparticles, NdFeB nanoparticles, and Fe foam.
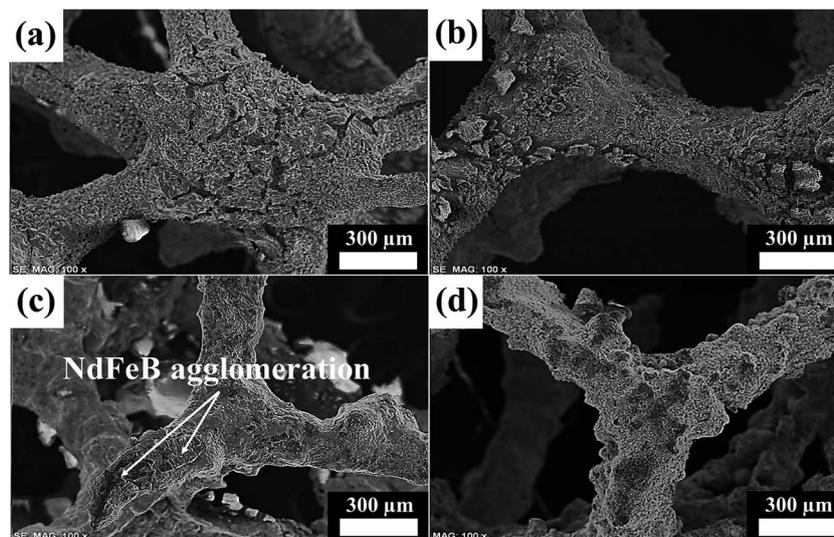
Fig. 6 SEM images of (a) original Fe foam, (b) NdNiAl nanoparticles, (c) NdFeB nanoparticles, and (d) NdNiAl and NdFeB hybrid nanoparticles coated on the surface of Fe foam.

the NdNiAl nanoparticles and the Fe foam. However, the catalytic nanoparticles were evenly distributed all over the template foam, which maintained its porous surface and thus possessed a large surface area.

After the subsequent electrospray coating and sintering processes of NdFeB nanoparticles over Fe foam, the surface morphology changed greatly. Fig. 6c provides an SEM image of the NdFeB nanoparticles dispersed over Fe foam with the resulting smooth surface and crack-blocked morphology. However, the EDS mapping analysis result (ESI Fig. 9†) clearly revealed the agglomerated morphology of the NdFeB nanoparticles, with clumped distribution, but also with tight consolidation on the Fe foam. Although it was possible to improve the uniformity of the magnetic coating layers by decreasing the concentration of the NdFeB nanoparticles, thick layers of the NdFeB nanoparticles were found to have still survived in the agglomerated state over the Fe foam. That is, the areas of magnetic sites were unevenly distributed, but strongly consolidated on the Fe foam.

As shown in Fig. 6d, almost all of the thick coating of catalytic and magnetic nanoparticles on the Fe foam was tightly adhered. The strong adhesion of the NdNiAl layers to the NdFeB nanoparticles already coating the Fe foam occurs primarily due to great magnetic strength. In a secondary manner to lower the surface energy of the nanoparticles, the van der Waals interaction also helped the nanoparticles to anchor and to interlock over the Fe foam. Previously, it was determined that the catalytic activity of the bimodal nanoparticles was improved due to the interfacial interaction between the NdNiAl and NdFeB nanoparticles. This was also related to the uniform dispersion of the catalytic nanoparticles. The SEM image revealed that the Nd phase of the NdFeB nanoparticles had close contact with the Nd phase of the NdNiAl nanoparticles at this interface. Simply because of this doping effect, there was a much higher probability of interconnection between the Nd phase of NdNiAl and

the Nd phase of NdFeB, as well more adhesion between the hybrid nanoparticles and the Fe foam *via* the magnetic strength of Nd. However, to obtain a uniform distribution of NdNiAl nanoparticles and to avoid severe agglomeration of the NdFeB nanoparticles, the concentration ratio between the two different nanoparticles should be carefully controlled, particularly when spraying the bimodal nanoparticles on the Fe foam. Overall, the SEM image shows that these catalytic and magnetic layers were uniformly distributed over the porous structure of the Fe foam. It was expected that this stable structure would be favorable for the reliable, rapid transformation of $CO + 3H_2$ to CH_4 during the catalytic reaction.

3.4. Catalytic and magnetic properties of NdNiAl nanoparticles supported by NdFeB nanoparticles

As shown in Fig. 7a, Nd-doped NiAl catalytic nanoparticles on the surface of NdFeB magnetic nanoparticles over Fe foam, exhibited a much higher CO conversion rate than the single mode catalysts, including the as-synthesized NdNiAl nanoparticles, the conventional NiAl RANEY® nanoparticles and the as-fabricated NdFeB nanoparticles over the same Fe foam. The initial CO conversion rate of NiAl nanoparticles was treated as a standard. Subsequently, when Nd was used as a dopant, NdNiAl nanoparticles had a comparatively higher CO conversion rate. Notably, the CO conversion rate, when catalyzed by the NdNiAl nanoparticles supported by NdFeB nanoparticles, was even higher than that of the single mode NdNiAl nanoparticles. This was because the employment of NdFeB nanoparticles imparted more homogeneous distribution to the NdNiAl nanoparticles *via* both strong magnetic force and relatively weak van der Waals interaction. It was also apparent that the higher catalytic rate of the bimodal (NdNiAl and NdFeB) nanoparticles was due to the catalytic kinetics of the metal–hydrogen interaction, which was mainly related to the high hydrogen absorptivity of NdFeB nanoparticles used as an
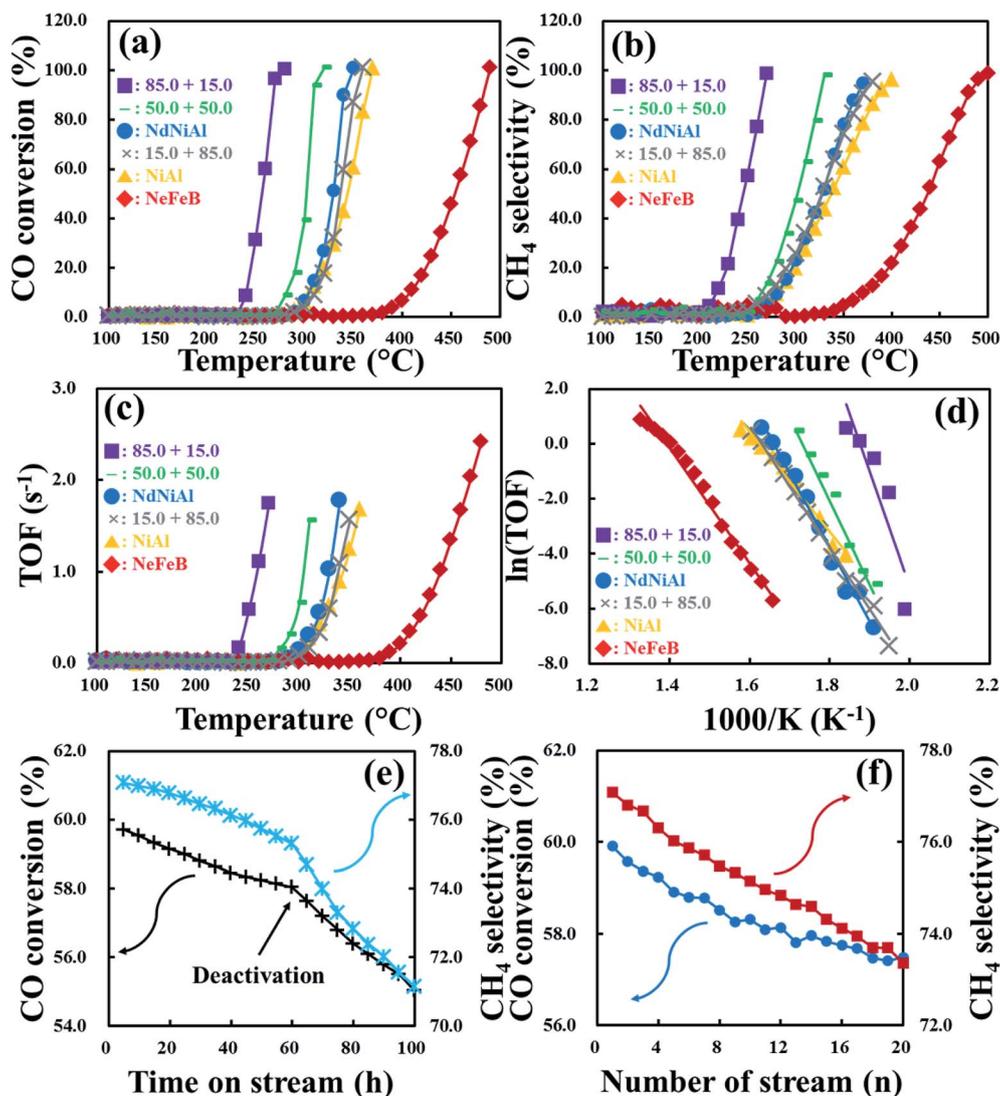
Fig. 7 CO conversion (a), CH$_4$ selectivity (b), turnover frequency (c), and Arrhenius plot (d) of the hybrid foam constituents over Fe foam: (■) 85.0 NdNiAl + 15.0 NdFeB nanoparticles, (—) 50.0 NdNiAl + 50.0 NdFeB nanoparticles, (●) NdNiAl nanoparticles, (×) 15.0 NdNiAl + 85.0 NdFeB nanoparticles, (▲) NiAl nanoparticles, and (◆) NdFeB nanoparticles. The CO conversion and CH$_4$ selectivity (e) for the hybrid NdNiAl–NdFeB nanoparticles (a ratio of 85.0 to 15.0 wt%) on Fe foam were measured at a specific temperature of 260 °C over a long period of time (from 0 to 100 h). The repeated CO conversion and CH$_4$ selectivity (f) of the hybrid foam were measured at the same temperature of 260 °C after being reactivated using the reactant gas composition of 80% H$_2$ and 20% He for 1 h at 700 °C.

assisting catalyst.[27,28] Regarding their thermodynamics, the Gibbs free energy changes for the hydrogenation and dehydrogenation of the NdFeB alloy at room temperature were ΔG_h = −143.2 mol^{-1} and ΔG_{dh} = −93.5 mol^{-1}, respectively.[28] Furthermore, the activation energy values for the hydrogenation and dehydrogenation of NdFeB were reported as 36.2 kJ mol^{-1} and 214–265 kJ mol^{-1}, respectively.[28] Thus, the energy barrier needs to be overcome to initiate hydrogenation. First, the most favorable Nd hydride and the thermodynamically stable NdFeB hydride were formed, corresponding to the hydrogenation state.[27] Afterward, the reaction temporarily paused during more nucleation and grain growth.[28] The crystal defects were reduced during the heat treatment, causing elevation of the surface energy level.[27,28] Subsequently, because the thermal energy

input was sufficient to allow the formation of metal hybrids during hydrogen absorption, the as-decomposed NdH$_{2+x}$, Fe$_2$B and α-Fe started to form.[27] Apparently, extending the hydrogenation time, imparted more NdFeB decomposition.[27] Although more energy input was necessary to overcome the activation energy barrier, which included activities related to atomic diffusion, breakage and formation of chemical bonds, the optimal conditions (thermodynamic and kinetic) presumably provide more frequent occurrence of such reactions.[28] Nonetheless, the NdFeB nanoparticles (in the presence of hydrogen) exhibited very active hydrogenation that effectively delivered hydrogen to the CO-activated NdNiAl nanoparticles.

To evaluate the catalytic efficiency of the NdNiAl nanoparticles in the presence of NdFeB nanoparticles, the CH$_4$

selectivity rates of the individual and hybrid types of nano-particles as a function of applied temperature are presented in Fig. 7b. First, the initial CH_4 selectivity of NiAl nanoparticles at 320.0 °C was 35.9%, while the CH_4 selectivity of NdFeB nano-particles at 460.0 °C was 72.6%. Then, the CH_4 selectivity of the NdNiAl nanoparticles at 320.0 °C was 42.2%, which was approximately 1.2 times higher than that of the NiAl nano-particles at the same temperature. The selectivity of the NiAl nanoparticles for producing CH_4 at 360.0 °C was 70.0%, whereas for CO hydrogenation catalyzed by NdNiAl nano-particles, this selectivity was 87.8%. This vast discrepancy was due to the presence of the $NdAl_2$ dopant phase, in addition to the Ni_3Al catalytic phase. Subsequently, the CH_4 selectivity rate of the NdNiAl nanoparticles in the presence of NdFeB nano-particles at 85.0 to 15.0 wt% ratio and 270.0 °C, was approxi-mately 20.5 times higher than that of the NdNiAl nanoparticles without the NdFeB nanoparticles support. As proven by the previous experiment, the catalytic activity of the NdNiAl nano-particles *via* the doping effect of Nd was increased by the intrinsic catalytic property of Nd phase, while the employment of the NdFeB nanoparticles in the presence of the NdNiAl nanoparticles imparted much better catalytic activity and selectivity due to their high hydrogen affinity.

Briefly, while the turnover frequency (TOF) of the NiAl nanoparticles as a standard at 360.0 °C was 1.7 s^{-1}, all of the NiAl nanoparticles and the NdNiAl–NdFeB hybrid nanoparticles with different ratios of catalysts showed a range of results, as shown in Fig. 7c. The NdFeB nanoparticles, which exhibited phase separation due to being prepared by the plasma treat-ment technique, also had relatively high catalytic activity of 2.4 s^{-1} at 480.0 °C due to their high hydrogen affinity. After the CO hydrogenation had proceeded at relatively low temperature; however, the maximum TOFs of CO + $3H_2$ into CH_4 for each NdNiAl–NdFeB hybrid nanoparticle were up to 1.7, 1.6, 1.8, and 1.6 s^{-1}, respectively. These were dependent on the concentra-tion ratio of NdNiAl nanoparticles to NdFeB nanoparticles (85.0 to 15.0, 50.0 to 50.0, 100.0 to 0.0, 15.0 to 85.0, and 0.0 to 100.0 wt%) as a function of the applied temperature. Thus, the cata-lytic activities of the NdNiAl nanoparticles dispersed using the magnetic force of the NdFeB nanoparticles, were on the order of 85.0 to 15.0 ≫ 50.0 to 50.0 > 100.0 to 0.0 > 15.0 to 85.0 ≫ 0.0 to 100.0 wt%. As a result, the increase of the catalytic activity and selectivity for the production of CH_4 was ascribed to the doping effect from Nd, given its intrinsic catalytic activity as a rare earth metal. Thereafter, the high hydrogen affinity obtained when using NdFeB nanoparticles resulted in a synergistic effect on the CO-activated NdNiAl nanoparticles. Overall, it was determined that the TOF of the hybrid nanoparticles immobilized on Fe foam depended on a synergistic increase in the interfacial interaction between the NdNiAl nanoparticles and NdFeB nanoparticles.

The Arrhenius plot (Fig. 7d) shows each turnover rate for the as-synthesized NdNiAl nanoparticles, the standard NiAl nano-particles, the as-fabricated NdFeB nanoparticles and each combination (NdNiAl–NdFeB) of hybrid nanoparticles over Fe foam. The corresponding rate determined the optimum oper-ation temperature for the bimodal NdNiAl–NdFeB hybrid

nanoparticles. It was also determined that optimization of 85.0 wt% NdNiAl nanoparticles supported by 15.0 wt% NdFeB nanoparticles loading imparted the highest catalytic activity and selectivity for the hydrogenation of CO to CH_4. This was because the high hydrogen reactivity of the NdFeB nano-particles influenced the CO hydrogenation of the NdNiAl nanoparticles to induce more rapid and effective CO + $3H_2$ conversion to CH_4.

Fig. 7e shows the durability of the hybrid NdNiAl–NdFeB nanoparticles (a ratio of 85.0 to 15.0 wt%) on Fe foam in terms of catalytic reaction over a long period of time (0 to 100 h). Specifically, the experiments were conducted to discover the life span of the catalyst with regard to the formation of carbide and oxide. During the initial catalytic activity of the fresh catalyst, there was CO conversion of 59.7% and CH_4 selectivity of 77.1%. Subsequently, both of the catalytic activities slowly deteriorated up to 60 h, then suddenly dropped and came to a halt at CO conversion of 55.0% and CH_4 selectivity of 71.1%.

To discover the recoverability of the hybrid foam, the cata-lytic activity for CO conversion and CH_4 selectivity was repeated 20 times after being reactivated before each cycle using a reac-tant gas composition of 80% H_2 and 20% He for 1 h at 700 °C, as shown in Fig. 7f. In comparison with the results of the above long time period of catalytic reaction, CO conversion and CH_4 selectivity of the hybrid foam deteriorated from 59.9% and 77.1% to 57.5% and 73.4%, respectively, due to the same deactivation process resulting in the formation of carbide and oxide. Thus, reduction in catalytic activity of the two processes by only 4.0% and 4.8% occurred even though the carbon deposition and oxide formation of the hybrid foam were sup-pressed by the hydrogen reduction process before each repeated cycle. However, the catalytic activities of the hybrid foam were continuously and gradually depressed but without significant deactivation despite a slight fluctuation between the 10th and the 14th cycle. As a result, the hybrid foam consisting of NdNiAl and NdFeB nanoparticles (a ratio of 85.0 to 15.0 wt%) consoli-dated on Fe foam had the highest catalytic activity at a low temperature of 270.0 °C (96.4% CO conversion, 98.5% CH_4 selectivity, and a TOF of 1.7 s^{-1}). In particular, the CH_4 selec-tivity of the single mode NdNiAl nanoparticles on Fe foam at 270.0 °C was 4.8%, which was approximately 20.5 times lower than that of the hybrid foam at the same temperature. Comparatively, the maximum catalytic activity of another hybrid foam consisting of NdNiAl and NdFeB nanoparticles (a ratio of 50.0 to 50.0 wt%) consolidated on Fe foam was achieved at a temperature above 330.0 °C. Thus, the composition of 85.0 NdNiAl and 15.0 NdFeB nanoparticles on Fe foam and at a temperature of 280 °C were the optimum conditions for CO hydrogenation and energy-saving.

Table 2 shows the BET results for each of the NdNiAl–NdFeB hybrid nanoparticles over Fe foam. Because the CO + $3H_2$ conversion reaction occurs mainly at the interfacial boundary between the catalytic nanoparticles and the magnetic nano-particles, the large surface area of the nanoparticles imparts better catalytic activity. As the concentration ratio of the NdNiAl nanoparticles to NdFeB nanoparticles increased, the surface area of the hybrid nanoparticles increased from 28.4 to 35.6 m^2

Table 2 BET results of hybrid foam constituents from top to bottom: Fe foam, NiAl nanoparticles, NdNiAl nanoparticles, NdFeB nanoparticles, 85.0 NdNiAl + 15.0 NdFeB nanoparticles, 50.0 NdNiAl + 50.0 NdFeB nanoparticles, and 15.0 NdNiAl + 85.0 NdFeB nanoparticles

	NdNiAl : NdFeB (wt% : wt%)	Loaded weight (g)	Surface area ($m^2\ g^{-1}$)	Atomic density (m^{-2})	Lattice plane ($h\ k\ l$)	T_{100} (°C)	Reference [n]
A	Fe	0.1008	0.2	1.72×10^{19}	Fe (1 1 0)	—	34
B	NiAl	0.1010	26.9	1.41×10^{19}	Ni (1 1 1)	370.0	33
C	NdNiAl	0.1012	28.4	1.41×10^{19}	Ni (1 1 1)	350.3	33
D	NdFeB	0.1006	20.8	1.72×10^{19}	Fe (1 1 0)	490.0	34
E	85.0 : 15.0	0.1009	35.6	1.46×10^{19}	0.85 Ni + 0.15 Fe	279.9	—
F	50.0 : 50.0	0.1007	34.9	1.57×10^{19}	0.50 Ni + 0.50 Fe	320.0	—
G	15.0 : 85.0	0.1006	29.9	1.67×10^{19}	0.15 Ni + 0.85 Fe	360.0	—

g^{-1}; however, their surface area certainly decreased. When only the NdFeB nanoparticles were present, their surface area was found to be 20.8 $m^2\ g^{-1}$. To be specific, the smaller size (21.8 nm) of catalytic nanoparticles filling the interval space among the relatively larger size (93.1 nm) of magnetic nanoparticles increased the surface area of the hybrid nanoparticles leading to the maximal activation area (35.6 $m^2\ g^{-1}$) for the absorption of $CO + H_2$. The high diffusivity of the catalytic nanoparticles also imparted a liquid-phase sintering effect among the magnetic nanoparticles.[43,50,51] Indeed, the catalytic nanoparticles, which existed at the surface boundaries or interstitial spaces among the magnetic nanoparticles, enhanced the distribution of small pores and the formation of strong cohesion among the hybrid nanoparticles during the heat treatment process.[43,52] However, the magnetic properties of the hybrid nanoparticles might have been lost above the Curie temperature despite the fact that the diffusion and consolidation of the hybrid nanoparticles on the Fe foam had already come to the end before reaching the temperature, which means that the adherence-assisting role of the magnetic nanoparticles to the Fe foam was no longer necessary. To be specific, in the initial stage of the heat treatment process, the hybrid nanoparticles became more viscous.[43,51,52] These changes were due to the catalytic nanoparticles in existence at the surface boundaries or interstitial spaces among the magnetic nanoparticles increasing their contacts. In the intermediate stage of the heat treatment process, drastic densification of the catalytic nanoparticles occurred on the surface of the magnetic nanoparticles where the interfacial boundary diffusion of the catalytic nanoparticles pre-dominated, thus increasing the diffusion reaction and forming the porous structure.[43,52] In this instance, the catalytic nanoparticles rapidly dispersed along the interstitial spaces among the magnetic nanoparticles and created many catalytic sites (more porous structures), thus enabling more gas absorption or desorption pathways (a wider surface area) inside the hybrid nanoparticles. The hybrid nanoparticles underwent completed attachment to the Fe foam during the final stage of the heat treatment. In terms of catalyst activation area, a remarkable bimodal effect of the hybrid nanoparticles was observed: the creation of a high surface area of 35.6 $m^2\ g^{-1}$ and fine surface morphology of the hybrid nanoparticles on the Fe foam, which uniformly imparted stronger hybrid nanoparticles/ Fe foam interactions. However, adding an excessive amount (85.0 wt%) of the magnetic nanoparticles to the catalytic

nanoparticles resulted in a decreased surface area (29.9 $m^2\ g^{-1}$) of the hybrid nanoparticles because the magnetic nanoparticles were larger with a much higher melting point (smaller diffusivity); the hybrid nanoparticles just experienced small grade sintering and necking without the capillary action of catalytic nanoparticles (the absence of the significant formation of a porous structure). Consequently, the hybrid nanoparticles consisting of 85.0 wt% catalytic nanoparticles and 15.0 wt% magnetic nanoparticles had the largest surface area of 35.6 $m^2\ g^{-1}$ and thus the highest catalytic activity and selectivity due to the formation of a more porous structure as a result of improved viscosity and diffusivity.

To investigate the magnetic strength of this hybrid material, magnetic hysteresis ($M \times H$) curves of the as-synthesized NdNiAl nanoparticles, the standard NiAl nanoparticles, the as-fabricated NdFeB nanoparticles, and the NdNiAl and NdFeB hybrid nanoparticles (at different concentration ratios) were recorded using a vibrating sample magnetometer with an applied field of −16 000 gauss < H < 16 000 gauss. The saturation magnetization, permanent magnetization, and magnetic coercivity for the single mode of each nanoparticle (NdNiAl, NiAl, and NdFeB) and their hybrid nanoparticles are shown in Fig. 8. The hysteresis loop also revealed that each one was super-paramagnetic at room temperature. To be specific, a saturation magnetization value (0.7 emu g^{-1}) of the NdNiAl nanoparticles was much lower than that of the NdFeB nanoparticles, which had a value of 6.1 emu g^{-1}. This value, compared to that of the NiAl nanoparticles, made sense considering the presence of Nd. The saturation magnetization of the $M \times H$ curve further indicated that the magnetic strength of only the NdNiAl nanoparticles, without the support of NdFeB nanoparticles, was not enough to impart strong adhesion to the Fe foam. This was because very weak saturation magnetization was shown for the NdNiAl nanoparticles, even though Nd was doped into the NiAl nanoparticles and had strong magnetic strength. However, the magnetic property of the NdFeB nanoparticles was appropriate for their application as a dispersion agent for the NdNiAl nanoparticles. The magnetic property allowed a layer of the former to serve as an intermediate supporter between the NdNiAl nanoparticles and the Fe foam. Compared to the coercivity of the NdFeB bulk material with the crystalline and anisotropic structure of the ordered intermetallic compound, the NdFeB nanoparticles had an unexpectedly low value, probably due to their amorphous structure and phase separation
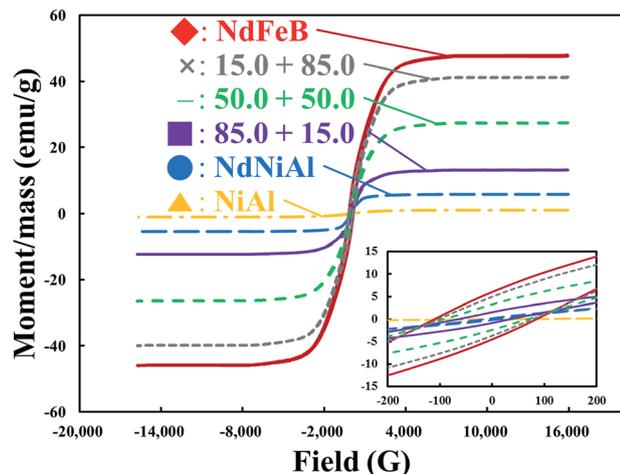
Fig. 8 Magnetic hysteresis plot of hybrid foam constituents from top to bottom: (◆) NdFeB nanoparticles, (×) 15.0 NdNiAl + 85.0 NdFeB nanoparticles, (−) 50.0 NdNiAl + 50.0 NdFeB nanoparticles, (■) 85.0 NdNiAl + 15.0 NdFeB nanoparticles, (●) NdNiAl nanoparticles, and (▲) NiAl nanoparticles. Magnetic feasibility test of hybrid foam constituents is shown in the inset of the plot. The inset highlights the coercivity of hybrid nanoparticles close to $M = 0$ emu g^{-1}.

caused by the plasma treatment using an evaporation–condensation method. However, the low magnetic strength was able to readily be enhanced by subsequent thermal recrystallization and anisotropic magnetization. Thus, the better magnetic properties of the NdFeB nanoparticles led to two main contributions: the NdFeB nanoparticles served as a dispersion agent and provided intermediate support thought to be responsible for the adhesion of the NdNiAl nanoparticles to the Fe foam. First, it took into account magnetic contribution to explain the uniform distribution of both types of nanoparticles on the Fe foam. Then, it demonstrated that the presence of the NdFeB nanoparticles (15.0 wt%) was necessary for strong magnetic adhesion because the NdNiAl nanoparticles, loaded at only 2.0 wt% of Nd, were insufficient to magnetically attach to the Fe foam, although the surface oxidation, phase separation, amorphous structure, and large surface-to-volume ratio of the magnetic nanoparticles had influenced the decrease of the saturation magnetization.[53] Compared to the coercivity value of the NdFeB nanoparticles (114.8 gauss), the NdNiAl nanoparticles exhibited a relatively low coercivity value of 12.1 gauss. As a result, our experimental results hinted that the NdFeB nanoparticles with great magnetic force had promoted the catalytic activity of the NdNiAl nanoparticles as a dispersion agent and intermediate supporter.

4. Conclusions

We developed a very effective heterogeneous catalyst system for the production of CH$_4$ by hydrogenation of CO using Nd-doped NiAl catalytic nanoparticles supported by NdFeB magnetic nanoparticles on Fe foam by a combination of chemical synthesis, physical fabrication, and a mechanical method. First, it was determined that the NdNiAl nanoparticles had higher

catalytic activity than that of the Nd-free, conventional NiAl RANEY® nanoparticles due to the synergistic effects of Nd. Then, the adoption of the NdFeB nanoparticles as an intermediate supporter and assisting catalyst imparted even higher catalytic activity and better conversion efficiency due to their strong magnetic force and high hydrogen affinity. Among the various combinations of NdNiAl and NdFeB nanoparticles, the catalytic activity of the bimodal nanoparticles as a function of the concentration ratio of NdNiAl to NdFeB nanoparticles was in the order of 85.0 to 15.0 ≫ 50.0 to 50.0 > 100.0 to 0.0 > 15.0 to 85.0 ≫ 0.0 to 100.0 wt%. The NdNiAl nanoparticles had an average size of 21.8 nm while the NdFeB nanoparticles had an average size of 93.1 nm; thus, the hybrid NdNiAl–NdFeB nanoparticles (a ratio of 85.0 to 15.0 wt%) consolidated on Fe foam had a higher surface area of 35.6 m^2 g^{-1} in the bimodal system with easy access to the catalytic active sites, which enhanced the absorption of reactant gases (CO + H$_2$) and the desorption of product gases (CH$_4$ + H$_2$O). Overall, the hybrid foam had the lowest temperature at 270.0 °C for 96.4% CO conversion and the similarly lowest temperature at 270.0 °C for 98.5% CH$_4$ selectivity. The hybrid foam had the highest TOF value of 1.7 s^{-1} at the same temperature, thus showed the steepest slope in an Arrhenius plot, which indicated highly effective CO conversion and efficient CH$_4$ selectivity compared to other single mode catalysts and nanoparticle combinations of the hybrid foam. As a result, the consolidation of the catalytic and magnetic nanoparticles over the template foam allowed the fabrication of the hybrid foam to be used as a core component in fuel cells or catalytic reactors for syngas utilization.

Author contributions

Sang Hoon Kim wrote and edited the paper and contributed to all activities. Joonphil Choi and Jaecheol Yun fabricated metal foam and analyzed the results. Joonphil Choi and Jaecheol Yun performed the fabrication of NdFeB nanoparticles using a plasma spraying system and analyzed their magnetic properties. Eun-wook Jeong synthesized NdNiAl nanoparticles and analyzed them using microscopic analysis methods. Sang Hoon Kim contributed to the interpretation and discussion of the experimental results.

Acknowledgements

References

1 S. Jeon, H. Roh, D. J. Moon and J. W. Bae, *RSC Adv.*, 2016, **6**, 68433–68444.
2 H. Xie, T. Lin, L. Shi and X. Meng, *RSC Adv.*, 2016, **6**, 97285–97292.
3 W. Li, Z. Zhao, P. Ren and G. Wang, *RSC Adv.*, 2015, **5**, 100865–100872.
4 K. H. Song, X. Yan, D. J. Koh, T. Kim and J. Chung, *Appl. Catal., A*, 2017, **530**, 184–192.

5 B. Höhlein, R. Menzer and J. Range, *Appl. Catal.*, 1981, **1**, 125–139.

6 M. Rahman, T. L. Church, M. F. Variava, A. T. Harris and A. I. Minett, *RSC Adv.*, 2014, **4**, 18951–18960.

7 E. Rahmi, A. A. Umar, M. Y. A. Rahman, M. M. Salleh and M. Oyama, *RSC Adv.*, 2016, **6**, 27696–27705.

8 W. Li, L. Kovarik, Y. Cheng, L. Nie, M. E. Bowden, J. Liu and Y. Wang, *RSC Adv.*, 2017, **7**, 3282–3286.

9 J. Chen, H. Zheng, J. Kang, F. Yang, Y. Cao and M. Xiang, *RSC Adv.*, 2017, **7**, 3035–3042.

10 A. Satsuma, M. Yanagihara, K. Osaki, Y. Saeki, H. Liu, Y. Yamamoto, S. Arai and J. Ohyama, *RSC Adv.*, 2014, **4**, 54187–54193.

11 G. Saravanan, R. Khobragade, L. C. Nagar and N. Labhsetwar, *RSC Adv.*, 2016, **6**, 85634–85642.

12 J. L. Lado, X. Wang, E. Paz, E. Carbó-Argibay, N. Guldris, C. Rodríguez-Abreu, L. Liu, K. Kovnir and Y. V. Kolen'ko, *ACS Catal.*, 2015, **5**, 6503–6508.

13 L. Bian, W. Wang, R. Xia and Z. Li, *RSC Adv.*, 2016, **6**, 677–686.

14 X. Chen, Y. Ma, L. Wang, Z. Yang, S. Jin, L. Zhang and C. Liang, *ChemCatChem*, 2015, **7**, 978–983.

15 M. Cokoja, H. Parala, A. Birkner, O. Shekhah, M. W. E. van den Berg and R. A. Fischer, *Chem. Mater.*, 2007, **19**, 5721–5733.

16 D. Giuranno, A. Tuissi, R. Novakovic and E. Ricci, *J. Chem. Eng. Data*, 2010, **55**, 3024–3028.

17 S. McFadden, R. S. Mishra, R. Valiev, A. Zhilyaev and A. Mukherjee, *Nature*, 1999, **398**, 684–686.

18 H. Modrow, M. Rahman, R. Richards, J. Hormes and H. Bönnemann, *J. Phys. Chem. B*, 2003, **107**, 12221–12226.

19 M. Pisarek, M. Łukaszewski, P. Winiarek, P. Kędzierzawski and M. Janik-Czachor, *Mater. Chem. Phys.*, 2009, **114**, 774–779.

20 G. Kwag, *Macromolecules*, 2002, **35**, 4875–4879.

21 F. Papa, L. Patron, O. Carp, C. Paraschiv and B. Ioan, *J. Mol. Catal. A: Chem.*, 2009, **299**, 93–97.

22 S. D. Bennett, S. J. Pope and B. D. Ward, *Chem. Commun.*, 2013, **49**, 6072–6074.

23 H. Sepehri-Amin, L. Liu, T. Ohkubo, M. Yano, T. Shoji, A. Kato, T. Schrefl and K. Hono, *Acta Mater.*, 2015, **99**, 297–306.

24 J. Roux and H. Grabke, *Appl. Surf. Sci.*, 1993, **68**, 49–63.

25 A. Mullis, T. Bigg and N. Adkins, *Intermetallics*, 2015, **67**, 63–68.

26 C. Leyens, B. Pint and I. Wright, *Surf. Coat. Technol.*, 2000, **133**, 15–22.

27 H. Sepehri-Amin, T. Ohkubo, K. Hono, K. Güth and O. Gutfleisch, *Acta Mater.*, 2015, **85**, 42–52.

28 X. Liu, L. Hu and Y. Mei, *Int. J. Hydrogen Energy*, 2013, **38**, 13694–13701.

29 X. Zou, Z. Rui, S. Song and H. Ji, *J. Catal.*, 2016, **338**, 192–201.

30 Y. C. Kimmel, L. Yang, T. G. Kelly, S. A. Rykov and J. G. Chen, *J. Catal.*, 2014, **312**, 216–220.

31 P. Serna and B. C. Gates, *Acc. Chem. Res.*, 2014, **47**, 2612–2620.

32 Y. Qian, P. Du, P. Wu, C. Cai and D. F. Gervasio, *J. Phys. Chem. C*, 2016, **120**, 9884–9896.

33 S. Yun, S. Lee, S. Yook, H. A. Patel, C. T. Yavuz and M. Choi, *ACS Catal.*, 2016, **6**, 2435–2442.

34 L. Xin, F. Yang, S. Rasouli, Y. Qiu, Z. Li, A. Uzunoglu, C. Sun, Y. Liu, P. Ferreira and W. Li, *ACS Catal.*, 2016, **6**, 2642–2653.

35 J. Liu, L. Cao, W. Huang and Z. Li, *ACS Appl. Mater. Interfaces*, 2011, **3**, 3552–3558.

36 M. A. Leon, R. Tschentscher, T. A. Nijhuis, J. van der Schaaf and J. C. Schouten, *Ind. Eng. Chem. Res.*, 2011, **50**, 3184–3193.

37 H. O. Seo, J. K. Sim, K. Kim, Y. D. Kim, D. C. Lim and S. H. Kim, *Appl. Catal., A*, 2013, **451**, 43–49.

38 C. Jung, J. Yun, K. Qadir, B. Naik, J. Yun and J. Y. Park, *Appl. Catal., B*, 2014, **154**, 171–176.

39 G. C. Bond, *Metal-catalysed reactions of hydrocarbons*, Springer, 2005.

40 G. Leibbrandt, P. Görts and F. Habraken, *Surf. Sci.*, 1991, **251**, 535–539.

41 S. H. Kim, K. N. Hui, Y. Kim, T. Lim, D. Yang, K. B. Kim, Y. J. Kim, G. J. Jang and S. Yang, *Mater. Des.*, 2016, **94**, 159–165.

42 S. H. Kim, K. N. Hui, Y. Kim, T. Lim, D. Yang, K. B. Kim, Y. J. Kim and S. Yang, *Corros. Sci.*, 2016, **105**, 25–35.

43 S. H. Kim, D. Yang, Y. Kim, T. Min, J. Choi, J. Yun, K. B. Kim, Y. J. Kim, J. H. Lee and Y. Do Kim, *Appl. Surf. Sci.*, 2016.

44 J. A. Haber, N. V. Gunda, J. J. Balbach, M. S. Conradi and W. E. Buhro, *Chem. Mater.*, 2000, **12**, 973–982.

45 R. Mohamed, *J. Alloys Compd.*, 2015, **648**, 711–718.

46 C. Powell, *J. Electron Spectrosc. Relat. Phenom.*, 2012, **185**, 1–3.

47 L. Hsu, Y. Wang and G. Guo, *J. Appl. Phys.*, 2002, **92**, 1419–1424.

48 I. Shabanova and V. Trapeznikov, *J. Electron Spectrosc. Relat. Phenom.*, 1975, **6**, 297–307.

49 D. S. Sundaram, P. Puri and V. Yang, *J. Phys. Chem. C*, 2013, **117**, 7858–7869.

50 L. Zhang and K. Tu, *Mater. Sci. Eng., R*, 2014, **82**, 1–32.

51 M. Son, I. Kim, S. Yang, T. Lee and H. Lee, *Microelectron. Eng.*, 2016, **164**, 128–134.

52 J. Choi, H. Lyu, W. Lee and J. Lee, *Powder Technol.*, 2014, **253**, 596–601.

53 J. Liu, H. Sepehri-Amin, T. Ohkubo, K. Hioki, A. Hattori, T. Schrefl and K. Hono, *Acta Mater.*, 2015, **82**, 336–343.